

September 2017’s Geoeffective Space Weather and Impacts to Caribbean Radio Communications during Hurricane Response

Robert Redmon^{1,1}, Daniel Seaton^{2,2}, Robert Steenburgh^{3,3}, Jing He^{4,4}, and Juan Rodriguez^{2,2}

¹National Centers for Environmental Information

²University of Colorado Boulder

³Space Weather Prediction Center

⁴Massachusetts Institute of Technology

November 30, 2022

Abstract

Between 4 and 10 September 2017, multiple solar eruptions occurred from active region AR12673. NOAA and NASA’s well-instrumented spacecraft observed the evolution of these geoeffective events from their solar origins, through the interplanetary medium, to their geospace impacts. The 6 September X9.3 flare was the largest to date for the nearly concluded solar cycle 24 and, in fact, the brightest recorded since an X17 flare in September 2005, which occurred during the declining phase of solar cycle 23. Rapid ionization of the sunlit upper atmosphere occurred, disrupting high frequency communications in the Caribbean region while emergency managers were scrambling to provide critical recovery services caused by the region’s devastating hurricanes. The 10 September west limb eruption resulted in the first solar energetic particle event since 2012 with sufficient flux and energy to yield a ground level enhancement. Spacecraft at L1, including DSCOVR, sampled the associated interplanetary coronal mass ejections minutes before their collision with Earth’s magnetosphere. Strong compression and erosion of the dayside magnetosphere occurred, placing geosynchronous satellites in the magnetosheath. Subsequent geomagnetic storms produced magnificent auroral displays and elevated hazards to power systems. Through the lens of NOAA’s space weather R-S-G storm scales, this event period increased hazards for systems susceptible to elevated “radio blackout” (R3-strong), “solar radiation storm” (S3-strong), and “geomagnetic storm” (G4-severe) conditions. The purpose of this paper is to provide an overview of the September 2017 space weather event, and a summary of its consequences, including forecaster, post event analyst and communication operator perspectives.

1 **September 2017’s Geoeffective Space Weather and Impacts to Caribbean**

2 **Radio Communications during Hurricane Response**

3 R. J. Redmon¹, D. B. Seaton^{1,2}, R. Steenburgh³, J. He⁴, J. V. Rodriguez^{1,2}

4 ¹National Centers for Environmental Information, NOAA, Boulder, CO, USA.

5 ²Cooperative Institute for Research in Environmental Sciences, Univ. of CO, Boulder, CO, USA.

6 ³Space Weather Prediction Center, NOAA, Boulder, CO, USA.

7 ⁴Massachusetts Institute of Technology and Woods Hole Oceanographic Institute Joint Program
8 in Oceanography and Applied Ocean Science and Engineering, Cambridge, MA, 02139 USA.

9 **Key Points**

- 10 1. The September 2017 solar events impacted high frequency radio links for ground and
11 aviation communication;
- 12 2. Radio communications used in hurricane emergency and disaster relief management were
13 affected, especially in the Caribbean;
- 14 3. Active Region AR12673 released 4 X-class flares, 3 coronal mass ejections and a solar
15 energetic particle event with ground level enhancement.

16

17 **Abstract**

18 Between 4 and 10 September 2017, multiple solar eruptions occurred from active region
19 AR12673. NOAA and NASA’s well-instrumented spacecraft observed the evolution of these
20 geoeffective events from their solar origins, through the interplanetary medium, to their geospace
21 impacts. The 6 September X9.3 flare was the largest to date for the nearly concluded solar cycle
22 24 and, in fact, the brightest recorded since an X17 flare in September 2005, which occurred
23 during the declining phase of solar cycle 23. Rapid ionization of the sunlit upper atmosphere
24 occurred, disrupting high frequency communications in the Caribbean region while emergency
25 managers were scrambling to provide critical recovery services caused by the region’s
26 devastating hurricanes. The 10 September west limb eruption resulted in the first solar energetic
27 particle event since 2012 with sufficient flux and energy to yield a ground level enhancement.
28 Spacecraft at L1, including DSCOVR, sampled the associated interplanetary coronal mass
29 ejections minutes before their collision with Earth’s magnetosphere. Strong compression and
30 erosion of the dayside magnetosphere occurred, placing geosynchronous satellites in the
31 magnetosheath. Subsequent geomagnetic storms produced magnificent auroral displays and
32 elevated hazards to power systems. Through the lens of NOAA’s space weather R-S-G storm
33 scales, this event period increased hazards for systems susceptible to elevated “radio blackout”
34 (R3-strong), “solar radiation storm” (S3-strong), and “geomagnetic storm” (G4-severe)
35 conditions. The purpose of this paper is to provide an overview of the September 2017 space
36 weather event, and a summary of its consequences, including forecaster, post event analyst and
37 communication operator perspectives.

38 **1 Introduction**

39 Space weather occasionally occurs in tandem with extreme terrestrial weather. When it does, the
40 struggle to mitigate the impacts to life and property can be dramatically intensified. This one-two
41 punch landed on the socioeconomically and technologically diverse communities of the
42 Caribbean islands during the September 2017 hurricane season. While hurricanes Harvey, Irma,
43 Jose and Maria tore through the Caribbean region, X-class flares, solar energetic particle (SEP)
44 events and Earth-directed coronal mass ejections (CMEs) plowed through the heliosphere.
45 Caribbean emergency communication system operators reported critical impacts to high
46 frequency (HF) radio links used in disaster response and aviation tracking. Unfortunate events
47 such as these provide an opportunity to expand our understanding of critical infrastructure
48 susceptibility to space weather. Such examinations are essential to prepare for and mitigate the
49 impacts of future events. (e.g. Baker et al., 2013; SWAP, 2015). Herein, we explore a diverse
50 suite of research and operational observations and model predictions to provide a comprehensive
51 summary of the evolution of the September 2017 solar eruptive period for the “Space Weather
52 Events of 4–10 September 2017” special collection of the *Space Weather Journal*. The
53 remainder of the manuscript is organized as follows: Section 2 provides an overview, Section 3
54 describes this space weather period from its solar eruptive origins to the near earth response,
55 Section 4 discusses technological impacts, and Section 5 provides a short summary.

56 **2 September Event Summary**

57 [Table 1](#) captures key space weather, geospace and technological impact details for the ten day
58 period 4–13 September 2017, all originating with solar active region AR12673. The content
59 includes the occurrence of solar flares ($\geq M5$), NOAA Space Weather Prediction Center (SWPC)
60 storm scale alerts for radio blackouts “R”, solar energetic particle (SEP) events “S”, geomagnetic

61 storms “G”, elevated fluxes of 2 MeV electrons at geosynchronous orbit, coronal mass ejections
 62 (CMEs), geostationary magnetopause crossings (GMCs), geomagnetic storm indices, spacecraft
 63 hazards, and technological system impacts. Events deemed “strong” are bold (e.g. storm scale
 64 level 3) and those deemed “severe” are bold-italic (e.g. storm scale level 4 and infrastructure).

65

66 Table 1: Summary of Space Weather 4-13 September 2017^a

(1) Date	(2) Flares ≥M5 (begin)	SWPC Storm Scales Alerts				(7) CME Earth- ward	(8) GMC GOES	(9) Geom. Indices (storm time)	(10) Space Haz	(11) System Impacts (Reported, Likely)
		(3) Radio (1–5)	(4) SEP (1–5)	(5) G (1–5)	(6) 2MeV e-					
Sep-4	M5.5 (20:28)	R2			Yes	Ejected (CME0)		Sep-8: Kp _{max} 8.3 Dst _{min} -142 nT (quick-look) -234 nT (predicted)	IC	
Sep-5			S2	G1	Yes				IC	
Sep-6	X2.2 (08:57) X9.3 (11:53)	R3	S2		Yes	Arrived (CME0) Ejected (CME1)			IC	<i>HF</i> <i>Ground</i> <i>(reported)</i> <i>HF</i> <i>Aviation</i> <i>(reported)</i>
Sep-7	M7.3 (10:11) X1.3 (14:20)	R3	S2	G3	Yes	Arrived (CME1)	Yes		IC	
Sep-8	M8.1 (07:40)	R2	S2	<i>G4</i>	Yes					IC
Sep-9					Yes				IC	
Sep-10	X8.2 (15:35)	R3	S3, Yes GLE72		Yes	Ejected (CME2)			IC SEE	<i>HF</i> <i>Ground</i> (reported)
Sep-11					Yes				IC SEE	
Sep-12			S2	G1	Yes	Arrived			IC	

Sep-13			S1	G1		(CME2)				
--------	--	--	----	----	--	--------	--	--	--	--

67 ^a The 11 columns are laid out thus: (1) date, (2) flares ($\geq M5$), (3) radio storm scale “R”, (4) solar
 68 radiation storm scale “S” and >100 MeV protons exceedance of 1 pfu (Yes or blank), (5)
 69 geomagnetic storm scale “G”, (6) 2 MeV electron alert, (7) CMEs, (8) GMC, (9) storm-time
 70 extrema in Kp and Dst, (10) space asset hazards, (11) system impacts. The Dst_{\min} “quick-look” is
 71 from the Kyoto World Data Center (WDC), and “predicted” is from LASP (Temerin and Li
 72 [2002, 2006]). For the three SWPC storm scales in columns 3–5, only the greatest space weather
 73 scale value is listed in cases where multiple same-category alerts were issued for a given day.
 74 Entries deemed “strong” are **bold** and those deemed “severe” are ***bold-italic***.
 75

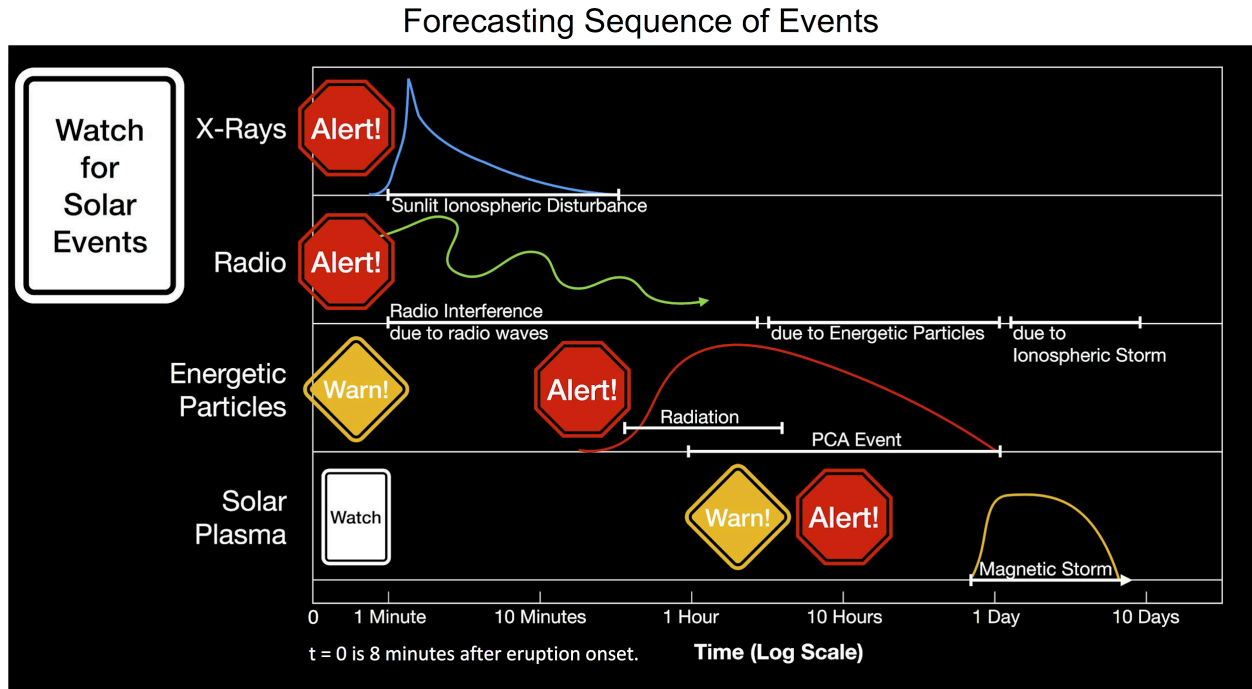
76 Through its eruptive evolution, AR12673 produced four X-class flares (column 2), with the most
 77 significant being an X9.3 on 6 September and an X8.2 on 10 September. In response, SWPC
 78 forecasters issued alerts for R3 “strong” radio blackouts (column 3). Reports of high frequency
 79 (HF) radio impacts were received from emergency communication providers such as the
 80 Hurricane Watch Net (HWN) and aviation interests such as the French Civil Aviation Authority
 81 (DGAC). The 10 September eruption resulted in the first SEP event with a ground level
 82 enhancement (GLE) near sea level since 2012 (Mishnev et al., 2017), now known as GLE 72
 83 (column 4). Several significant CMEs with at least partial earthward trajectories were emitted.
 84 Since this text is focused on the 6 and 10 September eruptions, we have named the CMEs as
 85 CME0 (4 September), CME1 (6 September) and CME2 (10 September) (column 7). The arrival
 86 of CME1 on 7-8 September heralded a very significant compression/erosion to the dayside
 87 magnetosphere, enough so to place geosynchronous spacecraft into the magnetosheath (column
 88 8). CME1 prompted a G4 “severe” SWPC alert (column 5) with a moderate overall geomagnetic
 89 storm (Kp_{\max} 8.3; Dst_{\min} -142 nT (quick-look), -234 nT (predicted; Temerin and Li [2002,
 90 2006])) (column 9). This period extends a fairly long run of elevated 2 MeV electrons (column
 91 6), known to be important for spacecraft internal charging considerations (column 10). The alert
 92 threshold was exceeded semi-continuously as far back as mid July, driven by several coronal

93 hole high speed streams resulting in Stream Interaction Regions (SIRs), which are common
94 during the declining phase of a solar cycle. For further context and study, see Luhmann et al.
95 (2018, their figure 3) and review OMNIWeb’s solar wind parameters and SWPC’s alerts timeline
96 (our Table 2).

97

98 For this paper we used data derived from National Oceanic Atmospheric Administration
99 (NOAA) SWPC and the National Centers for Environmental Information (NCEI), and National
100 Aeronautics and Space Administration (NASA) archives. All of these data are publicly available
101 (see [Table 2](#)). The knowledge accumulated in [Table 1](#) is afforded through collaboration and
102 leveraging of several key communities. Space weather practitioners must integrate disparate data
103 into a synthesis describing the current and future state of the space environment, distilling the
104 results with an eye towards the technological and societal impacts. They do this continuously
105 during their shift, across spatial and temporal scales spanning several orders of magnitude.
106 ([Figure 1](#)). Forecasters issue an *Alert* to “indicate that the observed conditions, highlighted by the
107 warnings, have crossed a preset threshold or that a space weather event has already started”, a
108 *Watch* “when the risk of a potentially hazardous space weather event has increased significantly,
109 but its occurrence or timing is still uncertain”, and a *Warning* “when a significant space weather
110 event is occurring, imminent or likely. A Warning is a short-term, high confidence prediction of
111 imminent activity.” (SWPC, 2018). In summary, [Table 1](#) is made possible by the real-time
112 SWPC forecaster synthesis of observations ([Figure 1](#)) from NOAA and NASA spacecraft ([Figure](#)
113 [2](#)) and ground platforms (e.g. magnetometers) into space weather alerts, watches and warnings;
114 the awareness of technology operators to report issues broadly for awareness and additional
115 perspective; and long term space environment scientific stewardship.

116



117

118

119

120

121

122

123

124

Figure 1: A forecaster’s timeline. SWPC and other forecasters are always watching for solar events as potential predictors of near-term technological impacts. This diagram provides a rough phenomenological timeline from X-ray and radio noise producing flares (top) to energetic particles (i.e., SEPs of both eruptive and CME origin) and the arrival of CME solar plasma. *Watches*, *Warnings* and *Alerts* are invaluable tools for forecasters to dissemination critical space weather information. Adapted from SWPC’s “Time Scale for Solar Effects”.

125 **3 Sun to Earth: Solar origins to Geospace response**

126

127

128

129

130

131

132

In this section, we present a Sun to Earth perspective, using data from several satellites ([Figure 2](#)). From our sunward observation location, the Lagrange point L1, we have solar imagery of the corona provided by NASA’s Solar and Heliospheric Observatory (SOHO) satellite; and in situ measurements of passing solar wind from the NOAA Deep Space Climate Observatory (DSCOVR) and the NASA Advanced Composition Explorer (ACE), SOHO, and Wind satellites. In geosynchronous orbit, NASA’s inclined (28.5°) Solar Dynamics Observatory (SDO) provides solar imagery of the disk, while NOAA’s Geostationary Operational Environmental Satellites

133 (GOES) provide solar imagery and in situ measurements of the penetrating and trapped particle
134 and magnetic field environment.

135

Solar Wind and Geosynchronous Observatories



136

137 Figure 2: Solar wind and geosynchronous observatories used in the present study. The nine
138 DSCOVR, ACE, SOHO, Wind, SDO, and GOES (G13–G16) satellite notional locations are
139 shown from the perspective of an observer looking down on the Sun-Earth ecliptic plane. At the
140 time of the September events studied here, the GOES spacecraft were located at these
141 approximate west geographic longitudes: 75 (G13), 90 (G16), 105 (G14), 135 (G15). The G16
142 SUVI image (left) captures the 10 September solar eruption (15:58 UT), while the DSCOVR
143 EPIC image (right) captures the Americas on 11 September 2017. (Image is not to scale.)

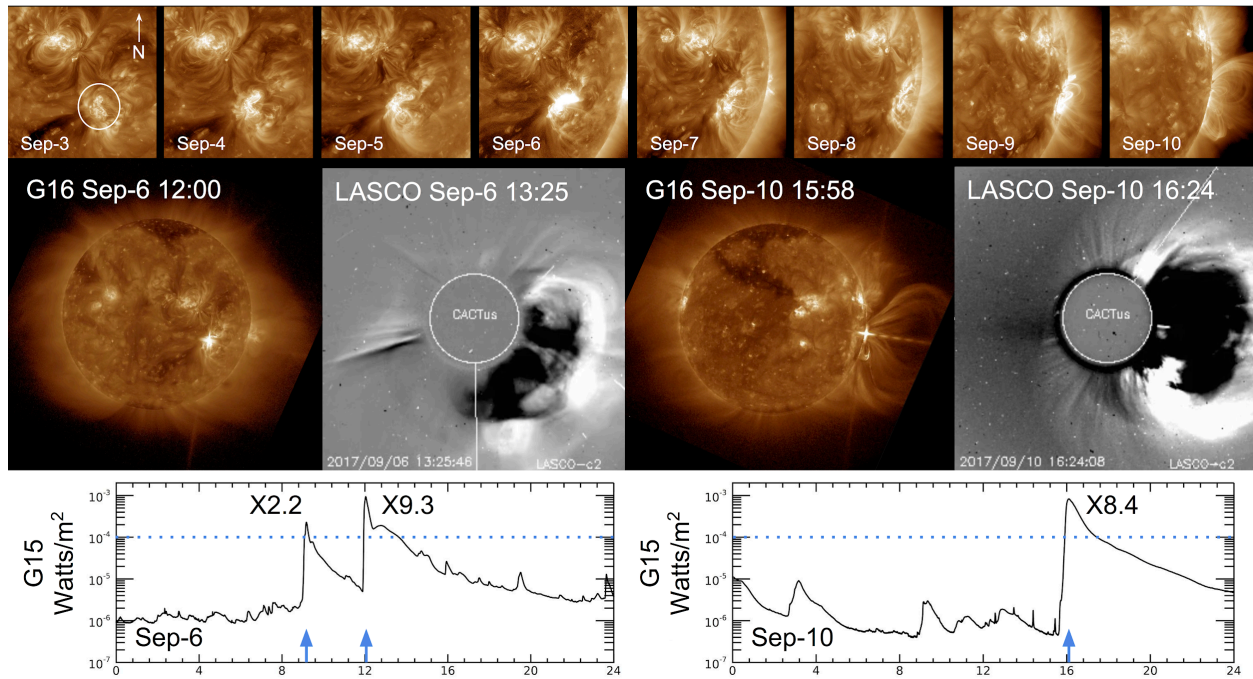
144

145 The early life of solar active region AR12673 was not initially suggestive of its rapid and
146 explosive evolution as it rotated across the solar disk. [Figure 3](#) reveals the time history of
147 AR12673 and its eruptive events on 6 and 10 September. The top row provides the eight day
148 time evolution covering 3–10 September from the SDO Atmospheric Imaging Assembly (AIA)
149 instrument, with AR12673 circled in the 3 September image. From 2 to 3 September, AR12673
150 expanded dramatically in both size — by roughly a factor of ten — and magnetic complexity.
151 Between 4 and 10 September, it fired off four X-class (X2.2, X9.3, X1.3, X8.2 in chronological
152 order) and numerous \geq M5 class flares (see [Table 1](#)). The two pairs of images in the middle row
153 show the solar disk at a wavelength of 195 Å from the new GOES-16 Solar Ultraviolet Imager
154 (SUVI) aboard GOES-16 and coronagraph images of ejecta from the SOHO Large Angle and
155 Spectrometric COronagraph (LASCO) (C2) for the 6 and 10 September events, respectively.

156 GOES-16 is the first in the NOAA GOES-R series of four spacecraft and was located at roughly
157 90° west geographic longitude for these events and most of 2017. The LASCO images reveal the
158 massive ejecta emitted on these days, with the 6 September eruption’s CME resulting in intense
159 magnetospheric compression and a G4 “severe” alert ([Figure 5](#) and [Table 1](#)). LASCO imagery
160 for the 6 September eruption (CME1) wasn't available to forecasters until approximately 6 hours
161 after the event, due to Deep Space Network (DSN) tracking prioritization. Providing operational,
162 real-time coronagraph imagery will ensure forecasters are able to analyze, model, and warn on
163 CMEs with minimal delay and maximum lead-time. The bottom row shows the matching X-ray
164 light curves observed by the GOES-15 X-ray Sensor (XRS) instrument’s “long” band (1 to 8 Å).
165 SWPC uses XRS measurements to determine the radio blackout scale (R) and these events
166 resulted in R3 “strong” alerts ([Table 1](#)). The SUVI images are taken at the time nearest to the X-
167 ray peaks for the given event. For model estimates of the propagation of these Interplanetary
168 CMEs (ICMEs) through the heliosphere see Luhmann et al. (2018; their figure 4). In particular,
169 the distinctly different trajectory and longitudinal extent near 1 AU for the 6 and 10 September
170 eruptions, respectively, correlate well with the G4 “severe” and G3 “strong” geomagnetic
171 disturbances observed at Earth. Similarly, they also help to describe the globally observed
172 Martian aurora following the 10 September eruption (NASA 2017). Collectively, this active
173 region’s explosive events on 6 and 10 September are the most energetic of solar cycle 24 (Seaton
174 and Darnel, 2018).

175

Evolution of AR12673



176
 177
 178
 179
 180
 181
 182
 183
 184
 185
 186
 187

Figure 3: The evolution and eruptions of Active Region AR12673. The top row shows the time evolution of AR12673 covering 3 September (circled) through 10 September by SDO AIA’s 193 Å telescope. The middle row shows the 6 and 10 September eruptive events as recorded by GOES-16 SUVI (195 Å) and SOHO LASCO (C2). SUVI images are after Seaton and Darnel (2018). The LASCO images were created using the Computer Aided CME Tracking CACTus package (Robbrecht and Berghmans, 2004). The bottom row reveals the X-ray light curves captured by GOES-15 XRS (0.1-0.8 nm “long”) covering 6 and 10 September and blue arrows mark the times of peak irradiance for the 3 X-class flares shown here. Brief outages of GOES-15 XRS near 9UT due to eclipse have been filled using GOES-13. The X1.3 flare on 7 September is not shown here.

188 Active region AR12673 erupted several times between 4 and 10 September, producing
 189 enhancements in the SEP population originating from the solar eruption site as well as
 190 energization by subsequent propagating ICMEs, resulting in several SWPC solar radiation storm
 191 scale “S” alerts ranging from moderate (S2) to strong (S3) ([Table 1](#)). In this manuscript we have
 192 chosen to use the terminology CME for discussions of the phenomena near their solar ejection
 193 and ICME to discuss phenomena related to their propagation further out. [Figure 4](#) shows GOES-
 194 13 measurements of the SEP protons penetrating through the geomagnetic field (top left) and
 195 trapped electrons (bottom left); and an evaluation of the GLE 72 event onset as observed by

196 multiple GOES spacecraft and ground based neutron monitors (NMs) (right column). The top
197 left plot shows proton fluxes in the energy range of >5 MeV to >100 MeV observed by the
198 GOES-13 Electron, Proton, Alpha Detector (EPEAD). The measurements from the westward-
199 viewing telescopes for EPEAD are shown here because they observe larger solar proton fluxes
200 than the eastward view due to the former seeing particles whose gyro centers lie outside
201 geosynchronous orbit and are hence less filtered by the geomagnetic field (e.g., Rodriguez et al.,
202 2010). Several SEP enhancements are annotated by their cause, solar eruption (September 4, 6
203 and 10) or CME1 or CME2 energized (September 7 and 8, and 12), in agreement with the
204 findings of Schwadron et al. (2018, this special collection) through their analysis of the Cosmic
205 Ray Telescope for the Effects of Radiation (CRaTER) detector. The period September 5–15
206 elevated the risks of astronaut radiation, space hardware Single Event Upsets (SEUs) and high
207 latitude trans-ionospheric radio absorption.

208

209 The eruption on 10 September propelled relativistic ions and electrons outward from AR12673
210 resulting in the first solar energetic particle (SEP) event with sufficient energy to yield a ground
211 level enhancement (GLE) in the count rates of secondary neutrons observed near sea level since
212 2012. This SEP event is now known as GLE 72 (<https://gle.oulu.fi/#/>). According to Schwadron
213 et al. (2018), GLE 72 “had an unusually hard spectrum, with large fluxes above 400 MeV, and
214 large dose rates in the most shielded CRaTER detector.” The CRaTER instrument is on the
215 Lunar Reconnaissance Orbiter (LRO) in orbit about Earth’s moon, and observes SEP events
216 essentially unfiltered by a planetary magnetosphere (Huang et al., 2009), unlike GOES.
217 Schwadron et al. provide concrete evidence that the multiple eruptions of AR12673 prior to 10
218 September created an interplanetary SEP seed population that was further energized by the 10

219 September eruption, in concurrence with past multi-CME studies (e.g. Li et al., 2012; Lugaz et
220 al., 2017). Luhmann et al. (2018) and Hassler et al. (2018; *in review*), of the same special
221 collection, have also evaluated this event near Mars. Luhmann et al. show good agreement
222 between the SEP event observed at Mars by the MAVEN (Mars Atmosphere and Volatile
223 Evolution) mission and the SEP MOD (SEP Model) (their figure 5) and that observer shock
224 connectivity explains these events well (see also their figure 4). Hassler et al. use Martian surface
225 observations from the Radiation Assessment Detector (RAD) instrument on the Mars Science
226 Laboratory (MSL) Curiosity rover to demonstrate that this is the strongest SEP event observed
227 since *Curiosity* deployed in 2012 and the first GLE to be observed simultaneously on two
228 planets.

229
230 Evaluation of GLE 72’s event onset detectability at Earth by GOES-13,14,15 and six NM ground
231 stations is presented in the right column of Figure 4. The technique used here for GLE 72 is the
232 same as that of He and Rodriguez (2018), who studied 17 GLEs, GLE 55 (November 6, 1997)
233 through GLE 71 (May 17, 2012) using an adaptation of the running-average detection method of
234 Kuwabara et al. (2006) designed to detect event onsets in noisy 1-min-cadence time series data,
235 and comprehensively concluded that neutron monitor and GOES observations detected similar
236 onset times; the 25th, 50th and 75th percentile differences being -1.5, 0, and +2.5 min when
237 GOES and NMs were compared using the same alert protocol. In the current study, we find that,
238 among the ensemble of measurements shown in Figure 4, GLE 72 was detected first by the
239 GOES-13 HEPAD P10 channel at 1618 UT, followed closely by the Fort Smith NM at 1619, the
240 GOES-14 HEPAD P9 and GOES-15 HEPAD P10 channels at 1620, and the EPEAD P7
241 channels on all three satellites at 1622. Interestingly, the next two NM detections were at 1648

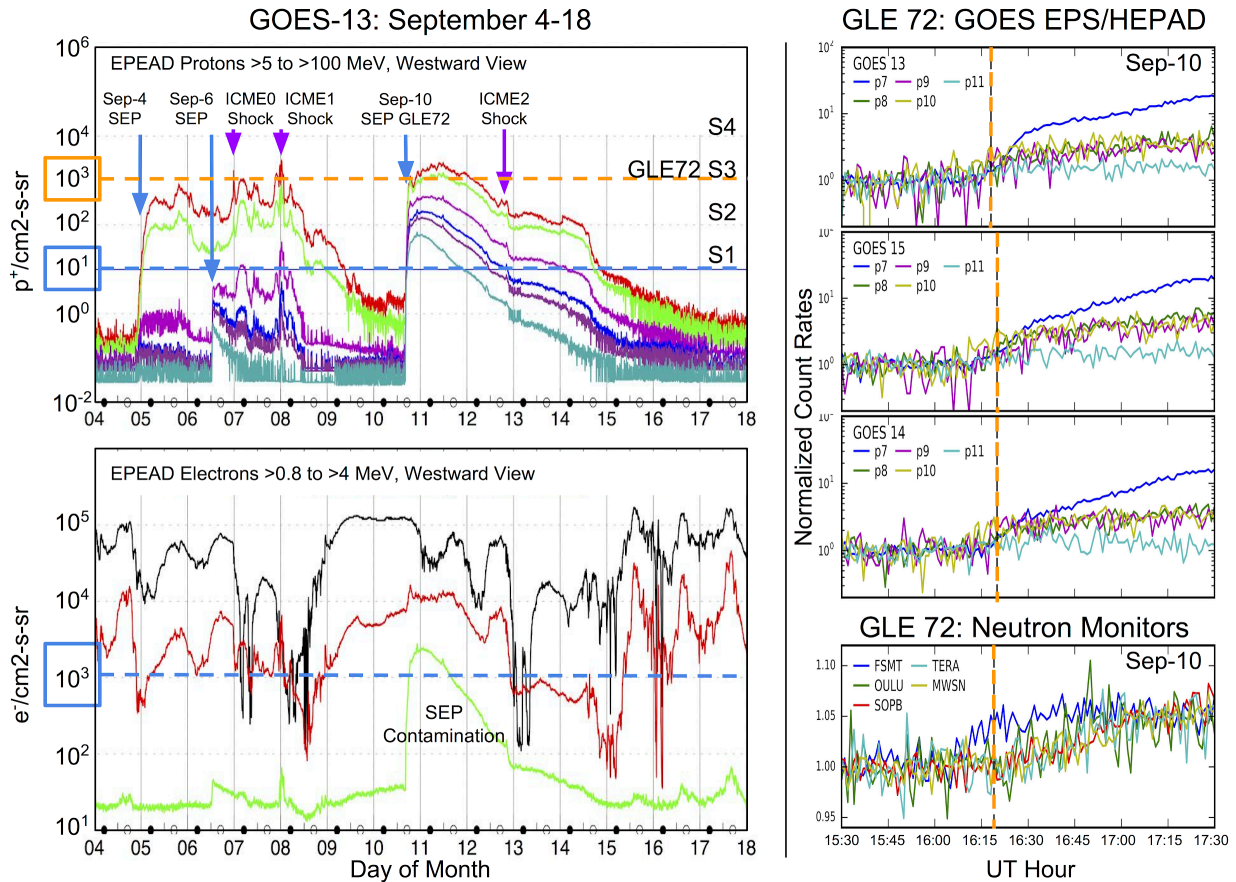
242 and 1652, by the Oulu and Terre Adélie NMs respectively, followed by South Pole Bares at
243 1657, and Mawson at 17:02. These delays with respect to the Fort Smith detection indicate a
244 pronounced anisotropy in the SEP event fluxes at onset.

245

246 Radiation belt electrons ([Figure 4](#) bottom left) were elevated for much of the 2017 summer, with
247 the SWPC alert threshold exceeded ($>2\text{MeV}$, $>1000\text{ pfus}$) semi-continuously as far back as mid-
248 July (see also section 2). The population was increased considerably (red trace enhancement on 8
249 September) by the moderate geomagnetic storm on 7–8 September ([Table 1](#)). Typical spacecraft
250 shielding can be penetrated by MeV electrons and thus spacecraft immersed in such
251 environments for long periods risk degradation and permanent damage through long term dose
252 and internal electrostatic discharge (Bodeau, 2010; Wrenn and Smith, 1996). It is worth pointing
253 out that the solar proton population on 10–12 September strongly contaminated the EPEAD
254 electron $>4\text{ MeV}$ channel measurements ([Figure 4](#), bottom left, green trace) and the $>2\text{ MeV}$
255 channel less obviously but still substantially. The contamination in these channels was smaller
256 though not negligible on 6–8 September. In contrast, the $>0.8\text{ MeV}$ channel was negligibly
257 contaminated by these SEP events and therefore can be used to monitor unambiguously the
258 evolution of the outer radiation belt at geostationary orbit throughout this period. The arrivals of
259 ICME0, ICME1, ICME2 and SIR1 on 6, 7, 13, and 14 September, respectively, caused dropouts
260 in the electron fluxes as expected (e.g., Onsager et al., 2007). Although the increase following
261 the storm on 7–8 September triggered by the first two ICMEs was substantial, as noted above,
262 the electron fluxes at all three energies (>0.8 , >2 and $>4\text{ MeV}$) increased to greater than pre-
263 event (4 September) levels following the arrival of SIR1. The dynamics of the magnetosphere
264 and the radiation belts in response to the arrival of these three ICMEs and one SIR is a rich case

265 deserving of in-depth study.

266



267

268 Figure 4: Solar energetic particles, GLE 72, and trapped electrons. The left column shows proton
 269 (top) and electron (bottom) fluxes for September 4–18 from the GOES-13 EPEAD westward
 270 directed telescope. The top figure shows protons for the 6 integral MeV energy ranges: >5 (*red*),
 271 >10 (*green*), >30 (*magenta*), >50 (*blue*), >60 (*purple*), and >100 (*cyan*). The 3 SEP event onsets
 272 from solar eruptions on 4, 6, and 10 September are indicated by vertical arrows, with the >10
 273 MeV channel (*green*) exceeding the SWPC S-scale S1 alert threshold for several days between
 274 5–15 September (inclusive) (*blue dashed*). The bottom figure shows electrons for the 3 integral
 275 MeV ranges: >0.8 (*black*), >2 (*red*), >4 (*green*, *SEP contaminated*). The dashed blue line here is
 276 the SWPC alert threshold for >2 MeV electrons (*red curve*). The right column depicts the
 277 September 10th, GLE-72 SEP event onset (*orange*) observed by GOES-13,14,15 and six NM
 278 ground stations from 15:30–17:30 UTC. The five GOES-13–15 channels shown here are from
 279 the EPS (P7, aka dome 5) and HEPAD (P8–P11, zenith directed telescope) instruments,
 280 collectively representing the nominal energy range >110 to >700 MeV. The five NMs are Fort
 281 Smith (FSMT), Oulu (OULU), South Pole Bares (SOPB), Terre Adélie (TERA), and Mawson
 282 (MWSN).
 283

284 As summarized in [Table 1](#), active region AR12673 ejected three CMEs during the period of 4–10

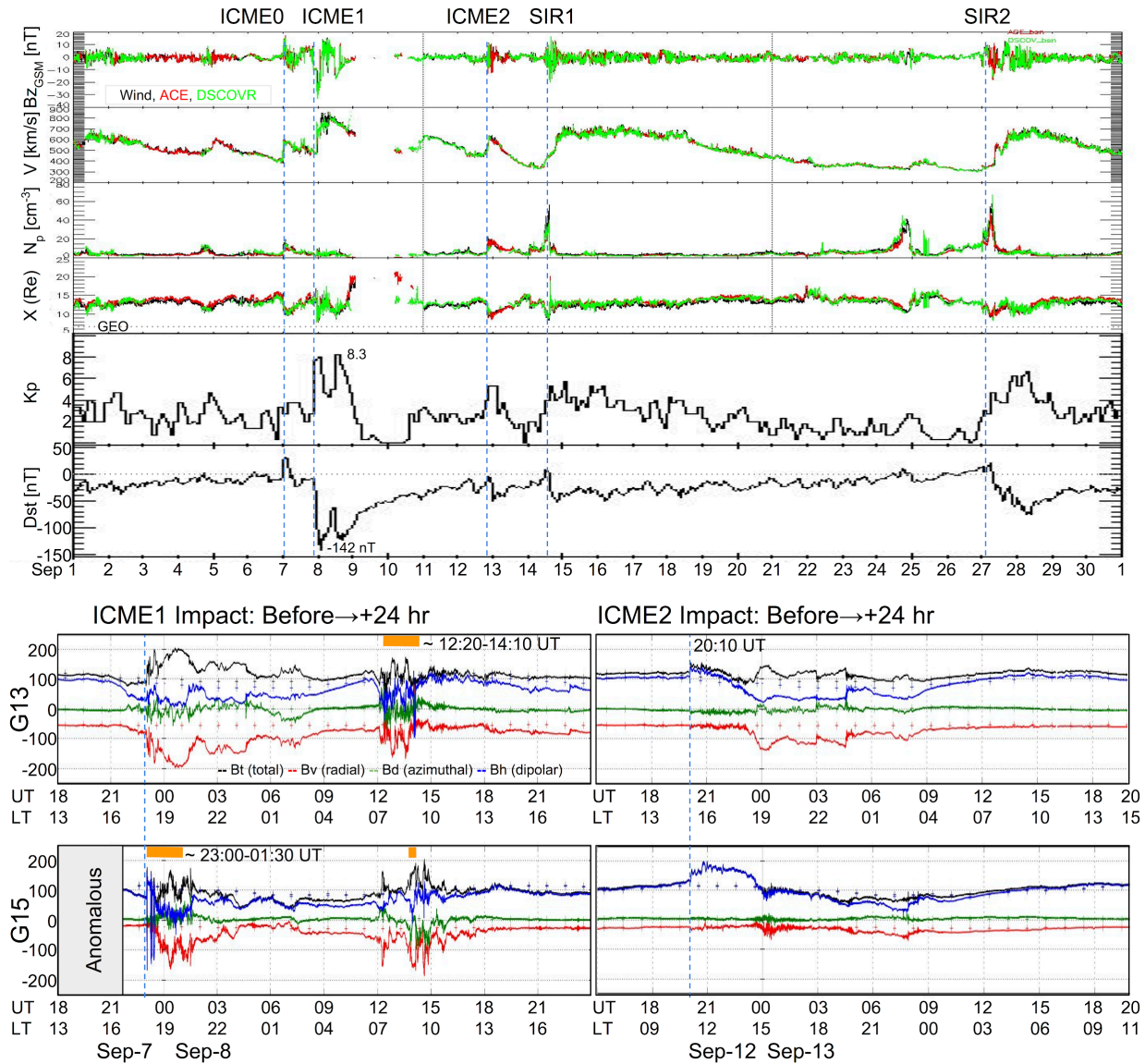
285 September. Their propagation through the interplanetary medium resulted in additional SEP
286 enhancements ([Figure 4](#)) and their impingement on geospace resulted in compression and
287 erosion of the magnetopause inward of geostationary orbit, a “severe” SWPC geomagnetic alert
288 (G4) and a moderate geomagnetic storm ($K_{p_{\max}}$ 8.3; Dst_{\min} -142 nT (quick-look), -234 nT
289 (predicted)). Observations of key solar wind bulk plasma parameters propagated to the bowshock
290 nose, the geomagnetic condition and the dayside magnetosphere response to ICME1 (arriving on
291 7 September) and ICME2 (arriving on 12 September) are captured in [Figure 5](#). The top four plots
292 are the bowshock plasma parameters: IMF Bz, flow speed, density, and the estimated bowshock
293 nose distance. The next two plots are the Kp and Dst indices. The vertical, dashed, blue lines
294 signal the arrive of ICMEs and SIRs at the bowshock nose. The 9 September bowshock data gap
295 is currently under investigation. As proxy for the solar wind condition during this outage, the
296 geomagnetic storm which peaked on 8 September, is well into recovery phase by the 9
297 September start of the outage. Finally, the lower quad of four plots shows the GOES-13 and
298 GOES-15 magnetic field in a dipole aligned frame. Several other geomagnetic indices (not
299 shown here) would also provide value for exploring this period of activity. For example,
300 measures of geomagnetic substorm activity, such as increases in the Auroral Electrojet (AE)
301 index (e.g., O'Brien et al., 2012) or substorm signatures at ground locations that are magnetically
302 conjugate to affected spacecraft (e.g., Farthing et al., 1982; Bodeau, 2015), could be used as an
303 indication of increased surface charging hazard for near-equatorial geosynchronous orbits
304 through the injection of energetic plasma. For the current period, the OMNIWeb AE index does
305 show several disturbed episodes nearing and exceeding 2000 nT (see Table 2 for access).

306

307 The arrival of ICME1 (7 September, second dashed line) resulted in compression and erosion of

308 the dayside magnetosphere, with the bowshock nose estimated to be $\sim 7.5 R_e$ (geocentric)
309 (fourth plot from top) (Farris, M.H. and C.T. Russell, 1994) and GMCs observed episodically by
310 GOES. These GMCs were observed for about 2.5 hours on the dusk flank at the 7 and 8
311 September boundary by GOES-15 (lower left plot, orange interval), and for about 1.8 hours later
312 on 8 September by GOES-13 (left, second from bottom) via the GOES magnetometer criteria (B_n
313 < 0 nT). The arrival of ICME2 (12 September, third blue dashed line) resulted in much less
314 predicted compression and erosion, and in concurrence, GOES-13 and GOES-15, which were
315 also on the dayside at the time of arrival, did not observe entry into the magnetosheath by the
316 same magnetometer criterion (lower right plots). The IMF B_z was much more southward and the
317 flow speed much stronger for the arrival of ICME1 (7 September) than for ICME2 (12
318 September) (topmost two plots). Looking forward to future capability, GOES-16’s new
319 Magnetospheric Particle Sensor-Low (MPS-LO) (Dichter et al., 2015) will provide electron and
320 ion density and temperature moments to improve the detection of GMCs beyond the traditional
321 criteria used here (i.e., Suvorova et al., 2005). The new moments and magnetopause location
322 products will be transitioned from NCEI and used operationally by SWPC (i.e., Petrinec et al.,
323 2017).
324

Solar Wind at the Bowshock and the Geomagnetic Response



325
 326 Figure 5: Solar wind at the bowshock and geomagnetic response for September, and GOES
 327 magnetic field response to ICME1 and ICME2 arrivals. The figure in the top half of this panel
 328 provides key interplanetary parameters shifted to the bowshock nose and the geomagnetic
 329 response for the full month of September (adapted from OMNIWeb) and the six plots in this
 330 panel from top to bottom are the B_z (GSM) component of the IMF, flow speed, proton density,
 331 bowshock nose distance (Re, geocentric), Kp and Dst (quick-look). The solar wind observing
 332 spacecraft (top 4 plots) are DSCOVR (green), ACE (red) and Wind (black). The approximate
 333 arrival times of key ICMEs and SIRs throughout September are labeled with dashed blue lines.
 334 At the start of the solar wind data gap Kp is ~ 2 and Dst is ~ -75 nT. The quad occupying the
 335 lower half of this panel shows the geosynchronous magnetic field response to the ICMEs
 336 arriving on 7 September (ICME1) and 12 September (ICME2) (dashed blue lines) as observed by
 337 GOES-13 and GOES-15. The coordinate frame is dipole field aligned (B_v : radial/poloidal (red),
 338 B_d : azimuthal/toroidal (green), B_h : dipolar/compressional (blue), B_t : total (black)). Plus ‘+’

339 symbols occurring hourly are the Olson-Pfizer quiet time model of the geomagnetic field
340 (OP77; Olson and Pfizer (1977)). Periods of dayside geosynchronous magnetopause crossings
341 determined by $B_h < 0$ are indicated by orange bars.
342

343 **4 Caribbean Radio Communication Impacts**

344 As Caribbean communities were responding to the 2017 hurricane season, the evolving active
345 region AR12673 erupted several times releasing X-class solar flares on September 6, 7, and 10
346 ([Table 1](#)). Rapid and comprehensive ionization of the equatorial upper atmosphere occurred,
347 disrupting HF communications while emergency managers were struggling to provide critical
348 recovery services (e.g. NCEI, 2017). Issues were reported by the Hurricane Weather Net (HWN),
349 and the French Civil Aviation Authority (DGAC).

350

351 Several news stories from the American Radio Relay League (ARRL) convey the Caribbean
352 radio operator perspective well. A few key excerpts are integrated here. Regarding the X9.3 flare
353 on September 6, HWN manager Bobby Graves reports: “In addition to the mix of three
354 hurricanes, the HWN has been hassled by a series of solar flares — one a massive Class X-9.3,
355 said to be the most powerful flare in more than a decade. ‘This solar flare caused a near-total
356 communications blackout for most of the morning and early afternoon,’ Graves recounted”
357 (ARRL, September 6, 2017). In consideration of the X8.2 flare on September 10, he further
358 implores: “As if Earth’s weather was not bad enough already, an X-class solar flare severely
359 disrupted HF communication on Sunday at around 1600 UTC. Graves said the widespread
360 communication blackout lasted for nearly 3 hours, ‘which could not have happened at a worse
361 time’” (ARRL, September 11, 2017). In addition to issues experienced by ground operators,
362 shortly after the September X9.3 solar flare, “French Civil Aviation authorities reported that HF

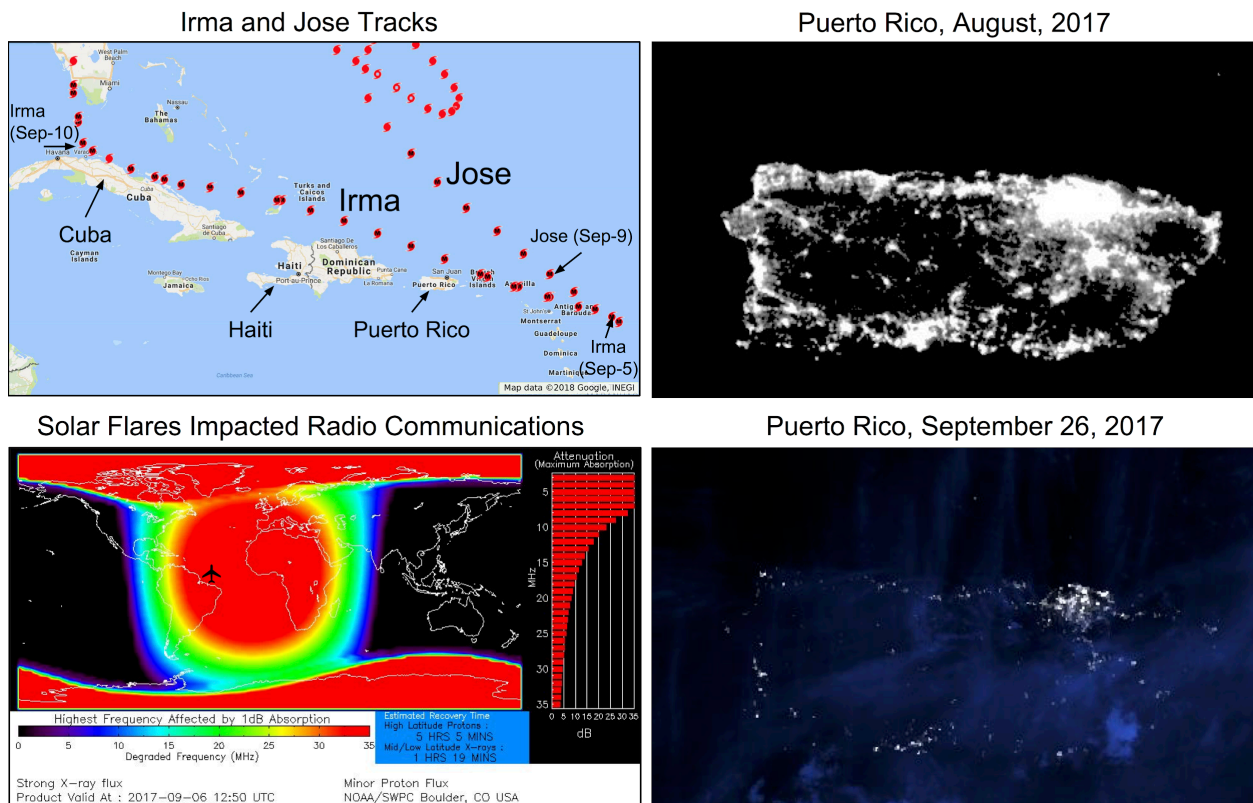
363 radio contact was lost with one non-Controller Pilot Data Link Communications (CPDLC)
364 equipped aircraft off the coasts of Brazil and French Guyana for approximately 90 minutes,
365 triggering an alert phase until a position report was received by New York radio” (French Civil
366 Aviation Authority to SWPC; Rutledge and Desbios, 2018).

367

368 [Figure 6](#) provides a graphical summary of the unfortunate alignment between terrestrial and
369 space weather during the 2017 hurricane season. The map on the upper left shows the paths of
370 Hurricanes Irma and Jose, which were ravaging the Caribbean during the solar eruptions of
371 AR12673. Hurricane Maria, whose eye passed directly over Puerto Rico, followed in mid to late
372 September. The map on the bottom left shows the location of the aforementioned aircraft HF loss
373 overlaid on the 6 September X9.3 flare radio blackout prediction using the D-Region Absorption
374 Prediction (DRAP) product (Sauer and Wilkinson, 2008). The right column provides maps
375 estimating the night-time lights as a power grid health proxy using the Suomi NPP Day Night
376 Band for August (top) and for late September after Hurricane Maria (bottom). Clearly, this
377 imagery gives a bleak view of post-hurricane Puerto Rico and the rest of the Caribbean. The
378 extraordinary sense of duty of the many relief effort contributors is well captured, once more by
379 Graves: “Considering the poor band conditions, not to mention the solar flares, members of the
380 Hurricane Watch Net persevered and did everything possible to help those in harm’s way”
381 (ARRL September 12, 2017).

382

Hurricane Season Worsened by Space Weather



383
384 Figure 6: Hurricane season issues worsened by solar eruptions. The top left figure depicts the
385 storm tracks of hurricanes Irma and Jose through the Caribbean (source: NWS data overlaid on
386 Google Maps; see Table 2). The bottom left figure provides an estimate of HF radio absorption
387 due to the 6 September solar eruption X9.3 flare and SEP using the DRAP model. The right
388 column shows an estimate of the night-time lights as a power grid health proxy using the Suomi
389 NPP Day Night Band for August (top) and for late September (bottom) (courtesy NCEI’s Chris
390 Elvidge and Kim Baugh).
391

392 Considering this period included the most energetic active region of solar cycle 24, with multiple
393 X-class flares, and multiple days of SWPC forecaster alerts at “severe” and “strong” levels, it is
394 anticipated that additional technological consequences will be reported in the future (e.g. the
395 long-lasting Geomagnetically Induced Currents (GICs) in New Zealand reported by Clilverd et
396 al. (2018, *in review*, this special collection)). For additional guidance evaluating the origins,
397 predictability, and consequences of space weather events using NOAA, NASA and other
398 research community tools, see Buzulukova (2018). In particular, evaluating potential

399 degradations to the U.S. Wide Area Augmentation System (WAAS) and the European
400 Geostationary Navigation Overlay Service (EGNOS) navigation aids due to the geomagnetic
401 storm (7–8 September) should be explored and is the subject of a future investigation. Similar to
402 the WAAS and EGNOS degradations concluded by Redmon et al. (2018a) in their evaluation of
403 geomagnetic storms in 2014 and 2015, maps of the Total Electron Content (TEC) from the
404 Madrigal service on September 7–8 show the development of significant TEC gradients and
405 EGNOS maps indicate service degradation relative to nearby non-storm days (see [Table 2](#) for
406 data access).

407 **5 Summary**

408 Multiple hurricanes carved destructive paths through the Caribbean during the 2017 hurricane
409 season, taking their toll on human life and critical infrastructure. The eyes of hurricanes Irma and
410 Jose passed slightly north of Puerto Rico, while Maria passed directly overhead. As a result, the
411 socioeconomically and technologically diverse communities of the Caribbean will collectively be
412 rebuilding and recovering for many years. This season, terrestrial and space weather collided,
413 exaggerating their individual consequences. AR12673 was the most energetic active region of
414 solar cycle 24, with its September 6th, X9.3 eruption, the most intense X-class flare recorded
415 since 2005, and its September 10th, X8.2 eruption, which produced the GLE 72 SEP event (most
416 energetic since 2012). These solar eruptions led to geoeffective space weather impacting radio
417 communications tools used in the management of air traffic as well as emergency-and-disaster
418 assessment and relief, temporarily complicating an already extreme terrestrial weather period.

419

420 Two generally important lessons learned from this period include the need to continue improving

421 forecaster access to operational, real-time coronagraph imagery (for solar ejecta monitoring), and
 422 the value of direct communication between forecast centers and customers during important
 423 space weather events to increase the awareness of space weather and technological impact
 424 causality. We have provided an overview of the September 2017 space weather event, and a
 425 summary of its consequences with forecaster, post event analyst and radio operator perspectives
 426 in order to aid future explorations between space weather, life and technology.

427

428 Table 2: Data source locations^a

Domain	Platform	Provider	Access
Solar Imagery	GOES-16	NCEI	https://www.ngdc.noaa.gov/stp/satellite/goes-r.html The SUVI data used in this study were created in a non-operational environment and are considered to be of “beta” maturity.
	SDO	NASA	http://www.jhelioviewer.org/
	SOHO	NASA	http://www.jhelioviewer.org/
Solar Wind	DSCOVR	NCEI	https://www.ngdc.noaa.gov/dscovr/portal/
	ACE, Wind, DSCOVR	NASA OMNIWeb	https://omniweb.sci.gsfc.nasa.gov/form/sc_merge_min1.html
Solar Energetic Particles	GOES SEM	NCEI	https://www.ngdc.noaa.gov/stp/satellite/goes/
	Neutron Monitors	NMDB	http://www.nmdb.eu/
Radiation Belts	GOES SEM	NCEI	https://www.ngdc.noaa.gov/stp/satellite/goes/
	POES/Metop SEM	NCEI	https://www.ngdc.noaa.gov/stp/satellite/poes/
	Belt Indices	NCEI	https://satdat.ngdc.noaa.gov/sem/poes/data/belt_indices/
Indices	Kp, Dst	NASA LASP	Dst “quick-look” and Kp (Figure 5): https://cdaweb.sci.gsfc.nasa.gov/index.html/ [This Dst “quick-look” is from WDC Kyoto]. Dst prediction: http://lasp.colorado.edu/space_weather/dsttemerin/archive/dst_2017_09.html
Ionosphere	DRAP	NCEI	https://www.ngdc.noaa.gov/stp/drap/

	Madrigal	MIT Haystack	http://madrigal.haystack.mit.edu/madrigal/experiments/2017/gps/08sep17/images/
Alerts	Radio, Radiation, Geomagnetic	SWPC	Scales: www.swpc.noaa.gov/noaa-scales-explanation Timeline: www.swpc.noaa.gov/products/notifications-timeline Alerts and Warnings Timeline: ftp.swpc.noaa.gov/pub/alerts/archive_20170901.html Events: ftp://ftp.swpc.noaa.gov/pub/indices/events/
Sun to Earth	Various	spaceweather.com	http://spaceweather.com/
Earth	DSCOVR EPIC	NASA	https://epic.gsfc.nasa.gov/?date=2017-09-12
Night Lights	Suomi NPP	NCEI	https://www.ngdc.noaa.gov/eog/interest/maria.html
Hurricane Reports	Reports	NWS	https://www.nhc.noaa.gov/data/tcr/
Aviation	WAAS	FAA	Top: http://www.nstb.tc.faa.gov/DisplayDailyPlotArchive.htm Events: http://ftp.nstb.tc.faa.gov/pub/NSTB_data/24HOURPLOTS/
	EGNOS	EDAS	Protection Level: https://egnos-user-support.essp-sas.eu/new_egnos_ops/protection_level LPV200: https://egnos-user-support.essp-sas.eu/new_egnos_ops/lpv200_availability Courtesy of ESSP and European GNSS Agency, produced under a program funded by the European Union

429 ^a From left to right, the columns provide: (1) domain or purpose, (2) observing platform or
 430 model, (3) provider, and (4) access method, after Redmon et al. (2018a).
 431

432

433 Acknowledgements

434 Two key NOAA organizations play roles that are critical to the U.S. and international space
 435 weather programs. SWPC provides data and information about the current and future state of the
 436 space environment and hazards products during elevated space weather conditions, helping to
 437 ensure the safety of life and property. The NCEI lab in Boulder, Colorado was known for

438 decades as the National Geophysical Data Center (NGDC) and World Data Center A (WDC-A).
439 NCEI’s Solar Terrestrial Physics program works very closely with SWPC and is currently
440 responsible for the calibration and validation of most of NOAA’s space environmental
441 instruments, the development of new products, the archival of key operational products used by
442 SWPC, the creation and dissemination of upgraded reference space environmental data records,
443 and interacting with other governmental and space physics research communities to optimize the
444 value and use of NOAA archives. The authors sincerely thank the many institutions and
445 individuals responsible for the Sun-to-Earth observations and predictions presented herein (see
446 [Table 2](#)) including NASA CDAWeb’s J. H. King and N. Papitashvili. The authors also wish to
447 specifically thank these individuals for valuable discussions: Bob Rutledge (SWPC), William
448 Rowland (NCEI DSCOVR data manager).

449
450 We acknowledge the NMDB database (www.nmdb.eu), founded under the European Union's
451 Seventh Framework (FP7) Programme (FP/2007-2013) under contract no. 213007, for providing
452 data. The neutron monitor data from Fort Smith are provided by the University of Delaware
453 Department of Physics and Astronomy and the Bartol Research Institute. The data from South
454 Pole Bares (SOPB) are provided by the University of Delaware with support from the U.S.
455 National Science Foundation under grant ANT-0838839. Terre Adélie neutron monitor data were
456 kindly provided by the French Polar Institute (IPEV, Brest) and by Paris Observatory. Oulu
457 neutron monitor data were kindly provided by the Sodankyla Geophysical Observatory. The
458 authors thank Dr Marc Duldig and the Australian Antarctic Division for providing the data from
459 the Mawson neutron monitor.

460 **References**

461 ARRL, “Hurricane Watch Net Now Watching Three Atlantic Basin Hurricanes”,
462 <http://www.arrl.org/news/hurricane-watch-net-now-watching-three-atlantic-basin-hurricanes>,
463 September 6, 2017.

464

465 ARRL, “Amateur Radio Volunteer Response Continues to Historic Hurricane Irma”,
466 [http://www.arrl.org/news/amateur-radio-volunteer-response-continues-to-historic-hurricane-](http://www.arrl.org/news/amateur-radio-volunteer-response-continues-to-historic-hurricane-irma)
467 [irma](http://www.arrl.org/news/amateur-radio-volunteer-response-continues-to-historic-hurricane-irma), September 11, 2017.

468

469 ARRL, “Hurricane Watch Net Currently Not Active but Still Eyeing José”,
470 <http://www.arrl.org/news/hurricane-watch-net-currently-not-active-but-still-eyeing-jos>,
471 September 12, 2017.

472

473 Baker, D.N., Li, X., Pulkkinen, A., Ngwira, C.M., Mays, M.L., Galvin, A.B., Simunac, K.D.C.,
474 2013. A major solar eruptive event in July 2012: defining extreme space weather scenarios.
475 *Space Weather* 11 (10), 585–591. <https://doi.org/10.1002/swe.20097>.

476

477 Bodeau, M., 2010. High Energy Electron Climatology that Supports Deep Charging Risk
478 Assessment in GEO, 2010–1608.

479

480 Bodeau, M. (2015), Review of Better Space Weather Proxies for Spacecraft Surface Charging,
481 *IEEE Trans. Plasma Sci.*, 43(9), 3075–3085, doi:10.1109/TPS.2015.2441038.

482

483 Buzulukova, N. Ed. (2018), *Extreme Events in Geospace: Origins, Predictability, and*

484 Consequences, Elsevier, doi:978-0-12-812700-1.

485

486 Clilverd, M.A., Rodger, C.J., Brundell, J.B., Dalzell, M., Martin, I., Mac Manus, D.H., Thomson,
487 N.R., Petersen, T., Obana, Y. (2018), Long-Lasting Geomagnetically Induced Currents and
488 Harmonic Distortion observed in New Zealand during the 07-08 September 2017 Disturbed
489 Period, *Space Weather, In Review*.

490

491 Dichter, B. K., Galica, G. E., McGarity, J. O., Tsui, S., Golightly, M. J., Lopate, C., et al. (2015).
492 Specification, design and calibration of the space
493 weather suite of instruments on the NOAA GOES-R program spacecraft. *IEEE Transactions on*
494 *Nuclear Science*, 62(6), 2776–2783.

495

496 Farris, M.H. and C.T. Russell, Determining the standoff distance of the bow shock: Mach
497 number dependence and use of models, *J. Geophys. Res.*, 99, 17681-17689, 1994,
498 doi:10.1029/94JA01020.

499

500 Hassler, D.M., Zeitlin, C., Ehresmann, B., Wimmer-Schweingruber, R.F., Guo, J., Matthiä, D.,
501 Rafkin, S., Berger, T., Reitz, G. (2018), Space Weather on the Surface of Mars: Impacts of the
502 September 2017 Events, *Space Weather, In Review*.

503

504 Huang, C.-L., H. E. Spence, and B. T. Kress (2009), Assessing access of galactic cosmic rays at
505 Moon's orbit, *Geophys. Res. Lett.*, 36, L09109, doi:[10.1029/2009GL037916](https://doi.org/10.1029/2009GL037916).

506

507 Kuwabara, T., J. W. Bieber, J. Clem, P. Evenson, and R. Pyle (2006), Development of a ground
508 level enhancement alarm system based upon neutron monitors, *Space Weather*, 4, S10001,
509 doi:10.1029/2006SW000223.

510

511 Li, G., R. Moore, R. A. Mewaldt, L. Zhao, and A. W. Labrador (2012), A Twin-CME
512 Scenario for Ground Level Enhancement Events, *Space Sci. Rev.*, 171, 141–160, doi:
513 10.1007/s11214-011-9823-7.

514

515 Lugaz, N., M. Temmer, Y. Wang, and C. J. Farrugia (2017), The Interaction of Successive
516 Coronal Mass Ejections: A Review, *Solar Phys.*, 292, 64, doi:10.1007/s11207-017-1091-
517 6.

518

519 Luhmann, J. G., Mays, M. L., Li, Y., Lee, C. O., Bain, H., Odstroil, D., et al. (2018). Shock
520 connectivity and the late cycle 24 solar energetic particle events in July and September 2017.
521 *Space Weather*, 16. <https://doi.org/10.1029/2018SW001860>.

522

523 Mishev, A., Poluianov, S., Usoskin, I., 2017. Assessment of spectral and angular characteristics
524 of sub-GLE events using the global neutron monitor network. *Journal of Space Weather and*
525 *Space Climate* 7, A28. <https://doi.org/10.1051/swsc/2017026>.

526

527 NASA, “Large Solar Storm Sparks Global Aurora and Doubles Radiation Levels on the Martian
528 Surface”, Available from: [https://www.nasa.gov/feature/jpl/large-solar-storm-sparks-global-](https://www.nasa.gov/feature/jpl/large-solar-storm-sparks-global-aurora-and-doubles-radiation-levels-on-the-martian-surface)
529 [aurora-and-doubles-radiation-levels-on-the-martian-surface](https://www.nasa.gov/feature/jpl/large-solar-storm-sparks-global-aurora-and-doubles-radiation-levels-on-the-martian-surface), Accessed 27 May 2018.

530

531 NCEI, National Oceanic and Atmospheric Administration, National Centers for Environmental
532 Information. (2017, September 17). Large Solar Event Detected During Irma. Retrieved from
533 <https://www.ncei.noaa.gov/news/large-solar-event-detected-during-irma>.

534

535 O'Brien, P., D. G. Brinkman, J. E. Mazur, J. F. Fennell, T. B. Guild (2012), A Human-in-the-
536 Loop Decision Tool for Preliminary Assessment of the Relevance, of the Space Environment to
537 a Satellite Anomaly, AEROSPACE NO. TOR-2011(8181)-2 Revision A.

538

539 Olson, W. P., and K. A. Pfizter (1977), Magnetospheric magnetic field modeling, Annual
540 Scientific Report, AFOSR contract F44620-75-C-0033, McDonnell Douglas Astronaut, Co.

541

542 Onsager, T. G., J. C. Green, G. D. Reeves, and H. J. Singer (2007), Solar wind and
543 magnetospheric conditions leading to the abrupt loss of outer radiation belt electrons, *J.*
544 *Geophys. Res.*, 112, A01202, doi:[10.1029/2006JA011708](https://doi.org/10.1029/2006JA011708).

545

546 Petrinec, S.M., Redmon, R.J., Rastaetter, L., 2017. Nowcasting and forecasting of the
547 magnetopause and bow shock—a status update. *Space Weather* 15 (1), 36–43.
548 <https://doi.org/10.1002/2016SW001565>.

549

550 Redmon, R. J., W. F. Denig, T. M. Loto'aniu, D. Fuller-Rowell 2018a, Recent Geoeffective
551 Space Weather Events and Technological System Impacts, In: *Extreme Events in Geospace*, Ed.
552 N. Buzulukova, Elsevier.

553

554 Robbrecht, E. and D. Berghmans (2004), Automated recognition of coronal mass ejections
555 (CMEs) in near-real-time data, *Astronomy and Astrophysics*, 425, 1097–1106,
556 <https://doi.org/10.1051/0004-6361:20041302>.

557

558 Rodriguez, J.V., Onsager, T.G., Mazur, J.E., 2010. The east-west effect in solar proton flux
559 measurements in geostationary orbit: a new GOES capability. *Geophys. Res. Lett.* 37, L07109.
560 <https://doi.org/10.1029/2010GL042531>.

561

562 Rutledge, R., Desbios, S. (2018), “Space weather focus: Impacts of a severe space weather event
563 on aviation operations”, World Meteorological Organization Commission for Aeronautical
564 Meteorology (CAeM) Newsletter, Issue 1/2018, Accessed on April 13, 2018,
565 <https://mailchi.mp/f7811e0713c9/wmo-caem-newsletter-issue-12018#Item%2019>.

566

567

568 Sauer, H.H., Wilkinson, D.C., 2008. Global mapping of ionospheric HF/VHF radio wave
569 absorption due to solar energetic protons. *Space Weather* 6, S12002.
570 <https://doi.org/10.1029/2008SW000399>.

571

572 Schwadron et al., (2018), Update on the worsening particle radiation environment observed by
573 CRaTER and implications for future human deep-space exploration, In Press,
574 <https://agupubs.onlinelibrary.wiley.com/doi/10.1002/2017SW001803>.

575

576 Seaton, D. B., and J. M. Darnel (2018), Observations of an Eruptive Solar Flare in the Extended
577 EUV Solar Corona, *The Astrophysical Journal Letters*, 852:L9 (7pp), doi:10.3847/2041-
578 8213/aaa28e.

579

580 “Space Weather Action Plan (SWAP)”, United States Office of Science and Technology Policy,
581 2015. Available from:

582 [https://obamawhitehouse.archives.gov/sites/default/files/microsites/ostp/final_nationalspaceweat](https://obamawhitehouse.archives.gov/sites/default/files/microsites/ostp/final_nationalspaceweatheractionplan_20151028.pdf)
583 [heractionplan_20151028.pdf](https://obamawhitehouse.archives.gov/sites/default/files/microsites/ostp/final_nationalspaceweatheractionplan_20151028.pdf), Accessed 1 January 2018.

584

585 Suvorova, A., Dmitriev, A., Chao, J.-K., Thoamsen, M., Yang, Y.-H., 2005. Necessary
586 conditions for geosynchronous magnetopause crossings. *J. Geophys. Res.* 110, A01206.
587 <https://doi.org/10.1029/2003JA010079>.

588

589 SWPC, “Space Weather Watches, Warnings and Alerts”, Available from:
590 <http://www.nws.noaa.gov/os/space/ww.shtml>, Accessed 2 April 2018.

591

592

593 Temerin, M., and X. Li, A new model for the prediction of Dst on the basis of the solar wind , *J.*
594 *Geophys. Res.*, 107(A12),1472, doi:10.1029/2001JA007532, 2002.

595

596 Temerin, M., and X. Li (2006), Dst model for 1995 –2002, *J. Geophys. Res.*, 111, A04221,
597 doi:10.1029/2005JA011257.

598

599 Wrenn, G.L., Smith, R.J.K., 1996. Probability factors governing ESD effects in geosynchronous
600 orbit. *IEEE Trans. Nucl. Sci.* 43, 2783–2789.

601

602

603